Nano Research 2013, 6(11): 795–807
DOI 10.1007/s12274-013-0358-y
Research Article

ISSN 1998-0124
CN 11-5974/O4

A novel strategy for improving upconversion luminescence of $NaYF_4$:Yb, Er nanocrystals by coupling with hybrids of silver plasmon nanostructures and poly(methyl methacrylate) photonic crystals

Wen Xu[1], Yongsheng Zhu[2], Xu Chen[1], Jing Wang[1], Li Tao[1], Sai Xu[1], Tong Liu[1], and Hongwei Song[1] (✉)

[1] *State Key Laboratory on Integrated Optoelectronics, College of Electronic Science and Engineering, Jilin University, 2699 Qianjin Street, Changchun 130012, China*

[2] *College of Physics, Jilin University, 2699 Qianjin Street, Changchun 130012, China*

Received: 30 May 2013
Revised: 29 July 2013
Accepted: 30 July 2013

KEYWORDS

upconversion,
porous Ag film,
near-field coupling,
opal photonic crystals (OPCs),
far-field coupling

ABSTRACT

The coupling of upconversion nanophosphors (UCNPs) with the surface plasmonic resonance (SPR) of noble metals is a promising way to improve luminescent efficiency of UCNPs; however, it is still a challenge to achieve stable, reproducible and effective upconversion luminescence (UCL) enhancement through such coupling. In this work, we present a novel strategy to improve UCL of $NaYF_4$:Yb^{3+},Er^{3+} UCNPs, by combining the near-field coupling of SPR of silver and the far-field coupling of poly(methyl methacrylate) (PMMA) opal photonic crystals (OPCs) with the UCNPs. In order to control the effective interaction distance between the UCNPs and the SPR, a porous silver film consisting of randomly distributed silver nanoparticles (NPs) (> 100 nm) was prepared which demonstrated strong SPR over a broad wavelength range, and its coupling to the UCNPs was found to be much stronger than that of a dense film. In the far-field coupling of OPCs, the photonic stop band (PSB) of the PMMA OPCs was tuned to 980 nm, matching exactly the excitation light. By modulating the particle size of the UCNPs, and the direction and excitation power of the incident light, a maximum enhancement of 60-fold was observed, which is an important advance for metal-induced UCL enhancement systems.

1 Introduction

In recent years, upconversion luminescence (UCL) of rare-earth (RE) doped nanophosphors has drawn considerable interest, due to their potential applications in lasers [1, 2], solar cells [3–5], biological fluorescence imaging and detection [6, 7], IR quantum counters [8], and display technologies [9]. Among various upconversion (UC) phosphors, bulk $NaYF_4$:Yb^{3+},Er^{3+} has been commonly considered as the most efficient

Address correspondence to songhw@jlu.edu.cn

under 980 nm excitation. However, based on previous reports in the Ref. [10], the luminescent quantum yield of a bulk sample is only 3%, and the UC efficiency is in the range of 0.005% to 0.3% for $NaYF_4$:20%Yb^{3+},2%Er^{3+} nanoparticles with particle sizes ranging from 10 to 100 nm. Therefore, it is important to enhance the luminescent efficiency of upconversion nanophosphors (UCNPs) in order to realize various applications. Up to now, various methods, such as suitable host selection, core–shell structure design and metal-induced enhancement effects, have been explored to amplify the UCL signals [11–16].

Plasmonic modulation of luminescence is a promising method for improving UCL [17–26]. As is well known, plasmonic nanostructures can concentrate the incoming light into strong localized electric fields that are distributed within the subwavelength regions close to the surface of the nanostructures. In general, the field enhancement is a near-field effect and decays nearly exponentially away from the metal surface [14]. Therefore, it is essential to control the effective coupling distance between the surface plasmon and nanophosphors. On one hand, if the density of metal NPs is not high enough—so that the spacing between neighboring NPs is larger than the size of the local field enhancement region—a large fraction of UCNPs will not interact with the metal NPs. On the other hand, in the vicinity of the plasmonic NPs, the plasmon resonance can alter both the re-radiative and nonradiative decay rates. The former process stimulates luminescent enhancement, while the latter process usually leads to quenching of photoluminescence. The nonradiative and re-radiation rates of the plasmonic NPs are essentially determined by their absorption and scattering cross sections at the emission wavelength [15]. When the size of metal NPs is relatively small (< 10 nm), although the interaction between metal NPs and nanophosphors is enhanced, the absorption cross section of the metal NPs will be increased considerably [23, 27], resulting in luminescent quenching. In metal NPs with relatively large sizes (> 100 nm), the scattering cross section is much larger than the absorption cross section of the NPs [27], which favors luminescence enhancement. In this work, in order to decrease the interaction distance between silver NPs and $NaYF_4$:Yb^{3+},Er^{3+} UCNPs, and improve the scattering of silver NPs, a porous silver film consisting of randomly distributed silver NPs (> 100 nm) was prepared and explored as a way of enhancing the UCL of $NaYF_4$:Yb^{3+},Er^{3+} UCNPs. The size of $NaYF_4$:Yb^{3+},Er^{3+} UCNPs was controlled in the range 6–50 nm in order to obtain an optimum enhancement.

Photonic crystals are materials with a periodically varying refractive index which have attracted extensive interest since the concept was first proposed in 1987, because they can control the propagation of electromagnetic waves and are of practical significance for photonic devices [28, 29]. They have frequently been used to modulate the emission wavelength, direction, radiative rate and intensity of some luminescent species, and have sometimes also been exploited to enhance the fluorescence intensity of phosphors [30, 31]. In this work, in order to further increase the UCL of $NaYF_4$:Yb^{3+},Er^{3+} UCNPs, we developed a novel device, combining the near-field coupling of a porous silver film with the $NaYF_4$:Yb^{3+},Er^{3+} UCNPs and the far-field coupling of three-dimensional poly(methyl methacrylate) (PMMA) photonic crystals (PCs) with the UCNPs.

It should also be highlighted that some reports have shown that hybrids such as core–shell structures can afford the near-field UCL enhancement of $NaYF_4$:Yb^{3+},Er^{3+}/Tm^{3+} through the coupling of RE ions to noble metal NPs (silver and gold) [19–21, 24]. However, most of these employed chemical control methods, which introduce some species, such as surfactants and solvents, that might significantly affect the intensity of UCL. Furthermore, in the solution phase, the distance between UCNPs and metal NPs is difficult to control, which leads to unstable and irreproducible UCL enhancement [16, 32]. The present work offers a way to obtain stable, reproducible UCL, and the porous film structure of the composites has the potential to be used directly in some photoelectric devices, such as upconverter solar cells, because of its excellent UCL characteristics and high transmission. It should be also noted that most of the previous work on plasmon-induced UCL enhancement concentrated on the coupling between Au NPs and the UCNPs, especially for those where super UCL enhancement was observed [20, 22]. The luminescent enhancement factors observed based on the coupling of silver

NPs with nanophosphors are typically only several-fold [18, 26, 33]. In the present work, we observe a maximum 50-fold UCL enhancement in the Ag NPs/$NaYF_4$:Yb^{3+},Er^{3+} UCNPs hybrids, and 60-fold UCL enhancement in the composites of PMMA OPCs/Ag NPs/$NaYF_4$:Yb^{3+},Er^{3+}UCNPs.

2 Results and discussion

2.1 Morphology and structure of porous Ag/$NaYF_4$:Yb^{3+},Er^{3+} hybrids

Different sizes of $NaYF_4$:Yb^{3+},Er^{3+} NPs were synthesized by a solvothermal method, as reported previously [34], and the porous Ag film was fabricated by a simple PMMA template removal method. The solvent evaporation method was used to assemble $NaYF_4$:Yb^{3+},Er^{3+} NPs layer-by-layer on the porous Ag film on a glass substrate [26]. Then, a PC was placed on the back of the glass substrate of the porous Ag/$NaYF_4$:Yb^{3+},Er^{3+} composite film. The preparation of the hybrid composed of PMMA opal photonic crystal (OPC), porous Ag film, and $NaYF_4$:Yb^{3+},Er^{3+} NPs is shown in Scheme 1(a). A more detailed description of the synthetic procedure and spectroscopy setup is given in the Electronic Supplementary Material (ESM). Transmission electron microscopy (TEM) images provide direct information about the size and typical shapes of as-prepared $NaYF_4$:Yb^{3+},Er^{3+} samples grown under different experimental conditions. Figures 1(a)–1(e) show the TEM images of $NaYF_4$ samples prepared at different temperatures. The average size of $NaYF_4$:Yb^{3+},Er^{3+} UCNPs increased and the products became more homogeneous as the preparation temperature increased. The average sizes of the $NaYF_4$:Yb^{3+},Er^{3+} UCNPs were determined to be 6, 13, 25, 35, and 50 nm, for the samples prepared at 285, 295, 305, 315 and 330 ℃, respectively. Figure 1(f) shows the X-ray diffraction (XRD) patterns of the as-prepared $NaYF_4$:Yb^{3+},Er^{3+} UCNPs and the porous Ag film and the standard cards of α-$NaYF_4$, β-$NaYF_4$ and cubic silver for comparison. It can be seen that the $NaYF_4$:Yb^{3+},Er^{3+} sample prepared at 285 ℃ adopts a cubic phase. As the reaction temperature increased to 295 ℃, there

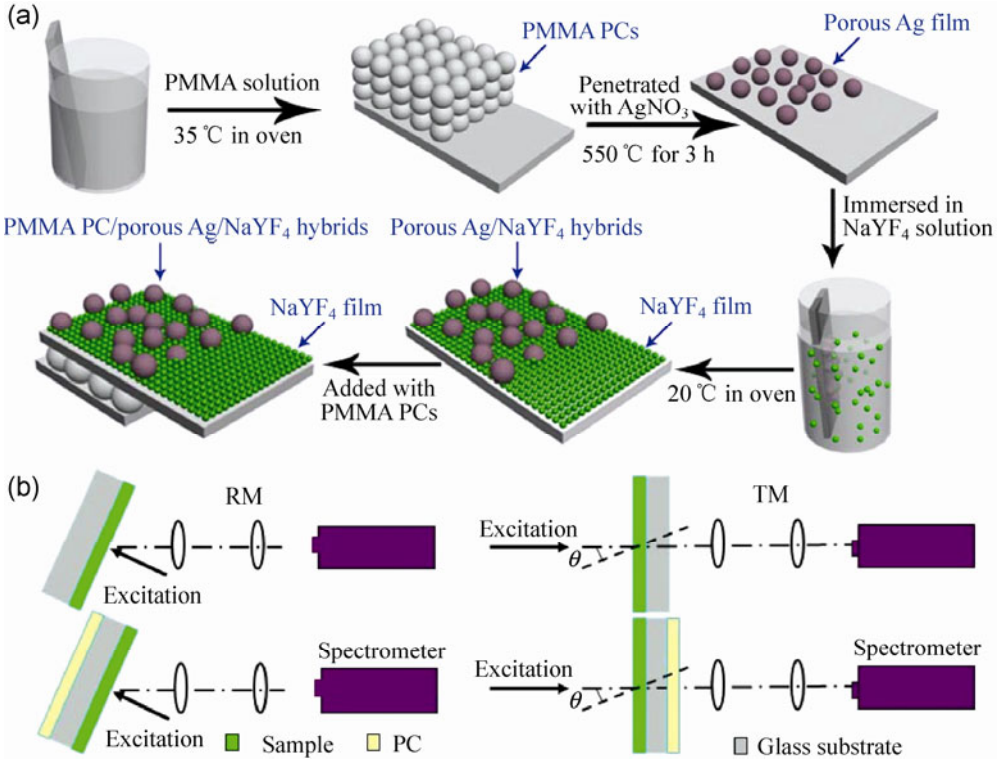

Scheme 1 (a) Schematic illustration of the PC/porous Ag/$NaYF_4$:Yb^{3+},Er^{3+} composite film formation process. (b) The two fluorescence measurement methods, namely reflection measurement (RM) and transmission measurement (TM).

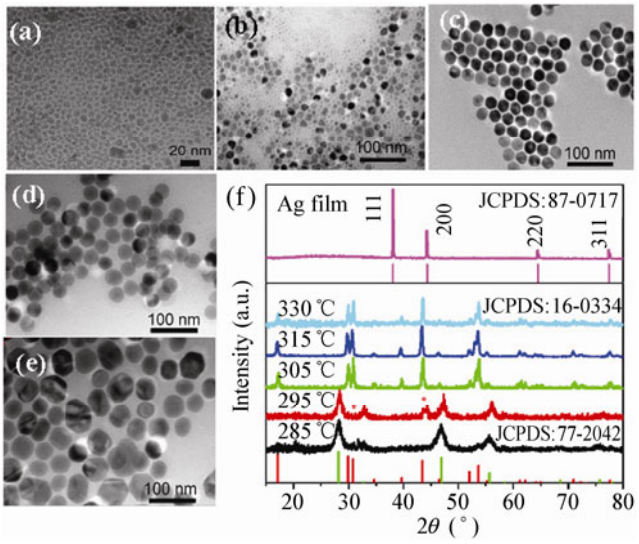

Figure 1 (a)–(e) TEM images of $NaYF_4$ samples prepared at different temperatures ranging from 285 to 330 ˚C. (f) XRD patterns of the as-prepared $NaYF_4$:Yb^{3+},Er^{3+} NPs fabricated at different temperatures and the porous Ag film with the standard cards for α-$NaYF_4$, β-$NaYF_4$, and cubic silver for comparison.

co-existed cubic and hexagonal phases, and on further increasing the temperature (> 305 ˚C), the $NaYF_4$ was completely transformed into the β-phase. For the porous Ag film, the peak positions were exactly in agreement with the standard pattern for cubic silver.

Figure 2(a) shows a scanning electron microscopy (SEM) image of the porous Ag film, which indicates that the Ag film is composed of randomly distributed and irregular Ag particles, ranging in size from 100–5,000 nm, with many pores among the Ag particles being formed during their annealing. Figure 2(b) shows a SEM image of $NaYF_4$:Yb^{3+},Er^{3+} film, indicating that a dense layer of $NaYF_4$:Yb^{3+},Er^{3+} particles with an average diameter of 25 nm was formed on the glass substrate. Figures 2(c) and 2(d) show low and high magnification SEM images of the porous Ag/$NaYF_4$:Yb^{3+},Er^{3+} film, respectively, where the Ag particles are marked with red circles, and parts of $NaYF_4$:Yb^{3+},Er^{3+} NCs are marked with red arrows. It can be seen that in the Ag/$NaYF_4$:Yb^{3+},Er^{3+} composite film, the $NaYF_4$:Yb^{3+},Er^{3+} UCNPs were formed in the pores between the Ag particles and on the surface of the Ag NPs, indicating the formation of hybrids. It is worth noting that in this hybrid no intervening layer (such as SiO_2, Al_2O_3) was introduced to keep the Ag and $NaYF_4$:Yb^{3+},Er^{3+} NPs apart [23, 24]. In order to further

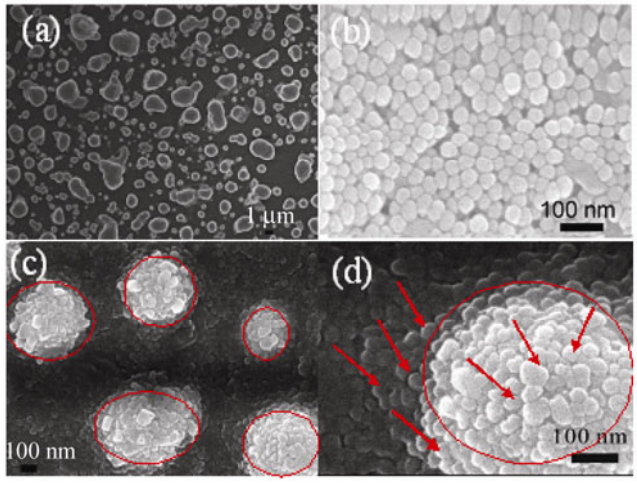

Figure 2 SEM images of the porous Ag film (a), $NaYF_4$:Yb^{3+},Er^{3+} film (b), and the low (c) and high (d) magnification images of the porous Ag/$NaYF_4$:Yb^{3+},Er^{3+} film.

determine the structure of the porous Ag/$NaYF_4$:Yb^{3+},Er^{3+} hybrid film, the hybrid was scraped from the glass substrate and dispersed in ethanol, then dropped onto a copper grid for high-resolution TEM (HR-TEM) measurements. Figures 3(a) and 3(b) respectively show low and high magnification HR-TEM images of Ag/$NaYF_4$:Yb^{3+},Er^{3+} hybrids. It can be clearly seen that the Ag particle was coated by $NaYF_4$:Yb^{3+},Er^{3+} UCNPs and the thickness of the surface $NaYF_4$:Yb^{3+},Er^{3+} layer on the Ag particle was in the range 30–150 nm. The fringes of a typical HR-TEM image (see Fig. 3(c)) of $NaYF_4$:Yb^{3+},Er^{3+} on the surface of the Ag particle (Fig. 3(b)) clearly show that in one particle the lattice was arranged along a single direction, and the lattice fringes have an interplanar spacing of 0.23 nm, which corresponds to the [111] spacing of hexagonal phase $NaYF_4$:Yb^{3+},Er^{3+}. The selected area electron diffraction (SAED) pattern recorded from the central $NaYF_4$:Yb^{3+},Er^{3+} NPs (Fig. 3(d)) reveals that the hexagonal phase $NaYF_4$:Yb^{3+},Er^{3+} has high crystallinity and is single crystalline in nature [34]. Energy-dispersive X-ray analysis (EDX, Fig. 3(e)) was also employed to measure the elemental composition of the hybrids and the result showed that the hybrids consisted of Ag in addition to Na, F, and Y, indicating that the Ag/$NaYF_4$:Yb^{3+},Er^{3+} hybrids were indeed formed. Overall, in the Ag/$NaYF_4$:Yb^{3+},Er^{3+} composite film, the $NaYF_4$:Yb^{3+},Er^{3+} UCNPs were mostly formed within the pores of the Ag film, resulting in decreasing

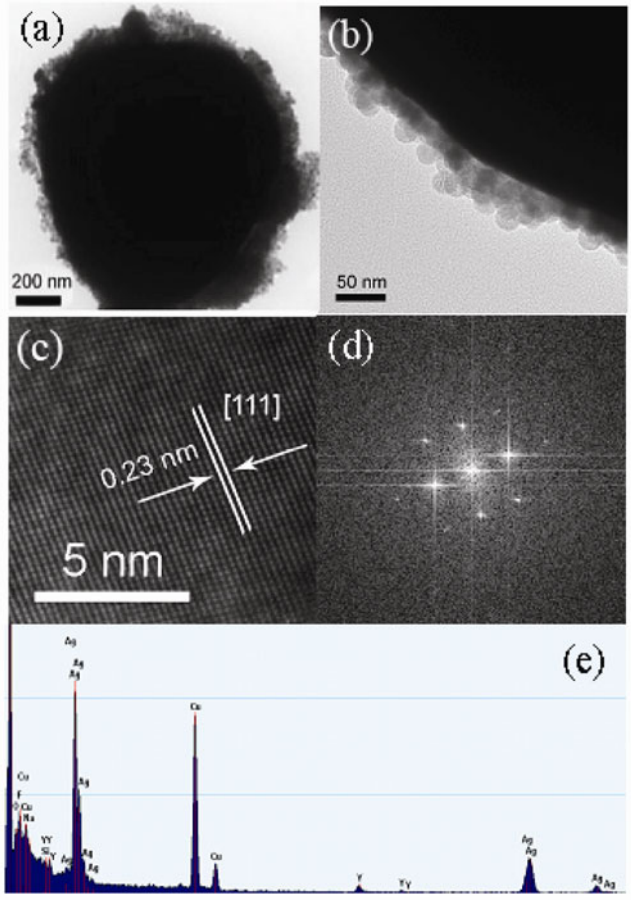

Figure 3 (a) Low and (b) high magnification HR-TEM images of porous Ag/$NaYF_4$:Yb^{3+},Er^{3+} hybrids. (c) A typical HR-TEM image of $NaYF_4$:Yb^{3+},Er^{3+} on the surface of an Ag particle. (d) The selected area electron diffraction (SAED) pattern recorded from the central $NaYF_4$:Yb^{3+},Er^{3+} NPs. (e) EDX analysis of porous Ag/$NaYF_4$:Yb^{3+},Er^{3+} hybrids.

interaction distance between $NaYF_4$ and silver plasmons, which is favorable for realizing effective near-field enhancement of UCL.

2.2 More effective UCL enhancement of porous Ag/$NaYF_4$:Yb^{3+},Er^{3+} hybrids

In this work, the UCL of $NaYF_4$:Yb^{3+},Er^{3+} UCNPs was measured in two different ways, namely reflection measurement (RM) and transmission measurement (TM), and their different optical paths are shown in Scheme 1(b). In the following text, measurement of the UCL spectra and dynamics employed the RM method, unless stated otherwise. Before the spectral measurement of UCL, the absorption spectra of the porous Ag film and the PMMA OPCs were characterized, as shown at the top of Fig. 4(a). A broad band extending from 350–1,100 nm was observed for the porous Ag film, which showed that the surface plasmon absorption (SPA) of the silver film arose from the contributions of both the transverse and longitudinal modes of localized SPAs owing to the irregular shapes of the silver NPs [35]. Strong plasmon coupling between the neighboring Ag NPs might also lead to the spectral broadening [36]. This allows the SPA of silver to couple with either the 980 nm excitation light or the emission lines of $NaYF_4$:Yb^{3+},Er^{3+}. The photonic stop band (PSB) of PMMA OPCs was centered at 980 nm, which exactly couples with the excitation field of $NaYF_4$:Yb^{3+},Er^{3+}. In order to better understand UCL enhancement, the typical UCL spectrum of $NaYF_4$:Yb^{3+},Er^{3+} and a schematic illustration of UC populating are provided in Figs. 4(a) and 4(b), respectively. It can be seen that the UCL of $NaYF_4$:Yb^{3+},Er^{3+} under 980 nm excitation includes the transitions $^2H_{9/2}$–$^4I_{15/2}$ at 410 nm, $^2H_{11/2}$–$^4I_{15/2}$ at 525 nm, $^4S_{3/2}$–$^4I_{15/2}$ at 546 nm, and $^4F_{9/2}$–$^4I_{15/2}$ at 660 nm. The green and red emissions come from two-photon processes, and the blue emission comes from a three-photon process [37].

In the porous Ag/$NaYF_4$:Yb^{3+},Er^{3+} hybrids, a remarkable UCL enhancement was observed in comparison with the $NaYF_4$:Yb^{3+},Er^{3+} film, and the magnitude depended strongly on the porous structure and the density of the Ag porous film. Figure 5(a) shows the UCL enhancement factors (EF) of a porous Ag/$NaYF_4$:Yb^{3+},Er^{3+} film and a dense Ag/$NaYF_4$:Yb^{3+},Er^{3+} film as a function of SPA strength at 980 nm, which is proportional to the density of the Ag film. EF represents the ratio of the total upconversion integrated intensity of the Ag/$NaYF_4$:Yb^{3+},Er^{3+} hybrids relative to the $NaYF_4$:Yb^{3+},Er^{3+} film, including $^2H_{9/2}$–$^4I_{15/2}$, $^2H_{11/2}$–$^4I_{15/2}$, $^4S_{3/2}$–$^4I_{15/2}$, and $^4F_{9/2}$–$^4I_{15/2}$ transitions. (The complete absorption spectra of porous Ag films with different densities of Ag NPs and the dense Ag film are shown in Fig. S1 in the ESM). Here, the 25 nm $NaYF_4$ was used for the preparation of the $NaYF_4$:Yb^{3+},Er^{3+} film and the Ag/$NaYF_4$:Yb^{3+},Er^{3+} composite film. It can be seen that EF of the porous Ag/$NaYF_4$:Yb^{3+},Er^{3+} film gradually increased from 1.2-fold to 14-fold with increasing Ag density. The EF of the dense Ag film was only 3.5-fold, although its density is much higher than those of the porous films. It can be deduced that,

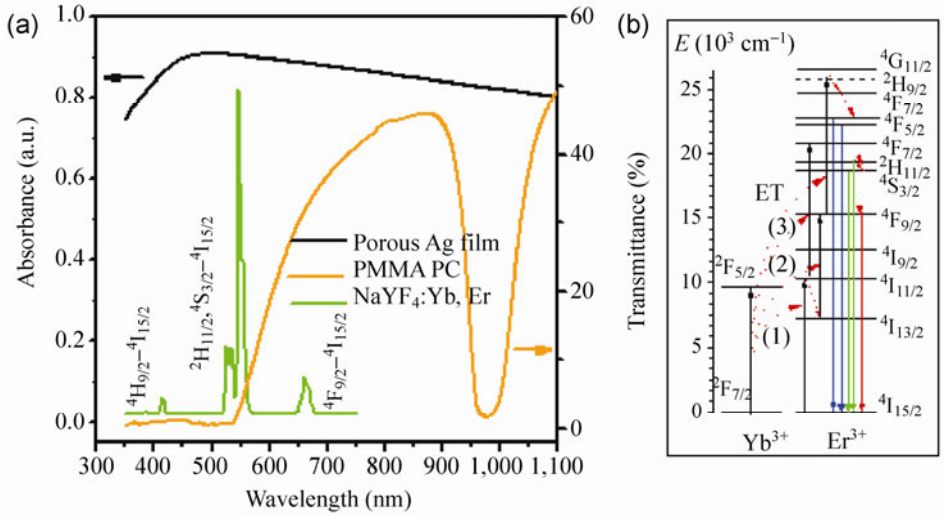

Figure 4 (a) The absorption spectrum of the porous Ag film, the transmittance spectrum of PC and the multicolor UC emissions of $NaYF_4:Yb^{3+},Er^{3+}$ film under 980 nm excitation. (b) The corresponding energy-level diagram of Yb^{3+}/Er^{3+}.

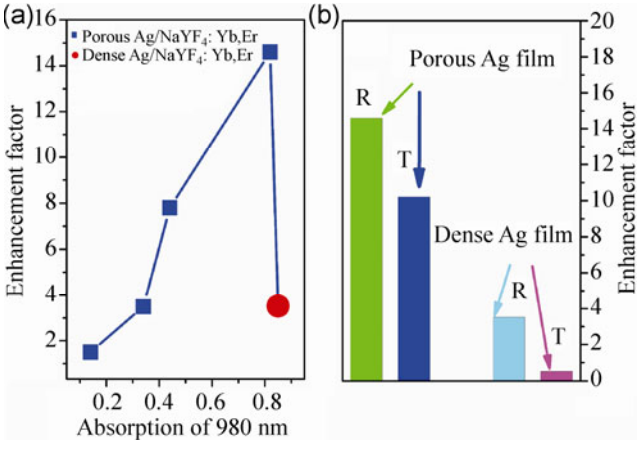

Figure 5 (a) The EFs of the porous and dense Ag/$NaYF_4$:Yb^{3+},Er^{3+} composite film as a function of the absorption of 980 nm light relative to the $NaYF_4:Yb^{3+},Er^{3+}$ (25 nm) film. (b) Comparison of EFs collected by RM and TM, respectively.

since the densities of silver are similar, the EF of the porous film is about four times that of the dense film, which can be attributed to the decreased distance between $NaYF_4:Yb^{3+},Er^{3+}$UCNPs and the surface plasmon of silver, resulting in stronger coupling. Figure 5(b) shows the EF of the porous Ag/$NaYF_4$:Yb^{3+},Er^{3+} film and the dense film, collected by RM and TM, respectively. It is interesting to observe that for the porous Ag film, UCL of $NaYF_4:Yb^{3+},Er^{3+}$ UCNPs could be enhanced for both RM and TM measurements, and the EFs are 14- and 10-fold, respectively. This implies that for the porous Ag/$NaYF_4:Yb^{3+},Er^{3+}$ film the UCL enhancement could be obtained in any direction, and the degree of UCL enhancement was only weakly dependent on the collection method. In contrast, for the dense film UCL enhancement could be only realized with RM (EF = 3.5), while with TM, UCL was considerably suppressed (EF = 0.5). The better UCL enhancement for the porous film may be related either to its stronger coupling with the UCNPs or its high transparency in the visible region.

In both the porous and dense Ag/$NaYF_4:Yb^{3+},Er^{3+}$ films, the UCL enhancements depend strongly on excitation power, however the trends are in opposite directions. Figure 6(a) shows the dependence of EF on the excitation power of 980 nm light. It can be seen that for the porous Ag/$NaYF_4:Yb^{3+},Er^{3+}$ composite film, the EF gradually increased from 14-fold to 18-fold as the excitation power was increased from 30 to 300 mW, while for the dense Ag/$NaYF_4:Yb^{3+},Er^{3+}$ composite film, the EF gradually decreased from 3.5-fold to 3.0-fold. In order to better understand this fact, the UCL integrated intensity of the green $^4S_{3/2}/^2H_{11/2}$–$^4I_{15/2}$ transitions as a function of excitation power was recorded, and a ln–ln plot is shown in Fig. 6(b). Generally, UCL intensity as a function of excitation power can be expressed as $I_{UCL} \propto P_{Laser}^{n}$ [38]. In Fig. 6(b), the slopes n of UCL are $n = 1.22$ for the pure $NaYF_4:Yb^{3+},Er^{3+}$ film, but slightly larger ($n = 1.32$) for the porous Ag/$NaYF_4:Yb^{3+},Er^{3+}$hybrid film and slightly

smaller (n = 1.15) for the dense Ag/$NaYF_4$:Yb^{3+},Er^{3+} film. The values of n are all much smaller than the required photon numbers (n = 2 or 3) to populate the corresponding levels, which can be attributed to saturation effects as well as the local thermal effects induced by the laser exposure [39]. The intensity ratio (R_{HS}) of $^2H_{11/2}$–$^4I_{15/2}$ to $^4S_{3/2}$–$^4I_{15/2}$ is sensitive to temperature and is a critical parameter in discussing the temperature change in UCL processes [38]. Figure 6(c) displays the deduced local temperature (based on R_{HS}) of the sample as a function of excitation power in different samples. It can be clearly seen that under the same excitation power the dense Ag/$NaYF_4$:Yb^{3+},Er^{3+} composite film demonstrated a much higher temperature increase than the $NaYF_4$:Yb^{3+},Er^{3+} film, and the porous Ag/$NaYF_4$:Yb^{3+},Er^{3+} composite film underwent only a slightly larger temperature increase relative to the $NaYF_4$:Yb^{3+},Er^{3+} film. Actually, the SPA of the silver films under 980 nm light induced extra and rapid photothermal transfer and thermal diffusion in the composite films, especially in the case of the dense film. We suggest that the variation of the slope n between different samples is related to the contribution of local thermal effects. The saturation effect, which causes n to deviate from the theoretical photon number, depends on the competition between linear decay and UC processes for the depletion of the intermediate excited states, as described theoretically by Pollnau et al. [40]. Based on this theory, if the linear decay is dominant, the slope will be 2, whereas if the UC is dominant, the slope will be 1. In the porous Ag/$NaYF_4$:Yb^{3+},Er^{3+} film, a moderate thermal effect resulted in an increase in the linear decay, leading to an increase in the slope n, while in the dense film, a strong thermal effect leads to a significant increase in nonradiative relaxation and the thermal quenching of UCL results in the decrease of n [41]. Thus, the porous Ag film can not only realize higher UCL enhancement than the dense Ag film, but also has a lower photothermal effect.

2.3 Dependence of UCL enhancement on particle size and incident angle

The size-dependence of the multicolor emissions (collected by RM and TM) of the $NaYF_4$:Yb^{3+},Er^{3+} nanofilm, and the porous Ag/$NaYF_4$:Yb^{3+},Er^{3+} and PMMA/Ag/$NaYF_4$:Yb^{3+},Er^{3+} composite films under the same conditions was investigated. Figures 7(a) and 7(b)

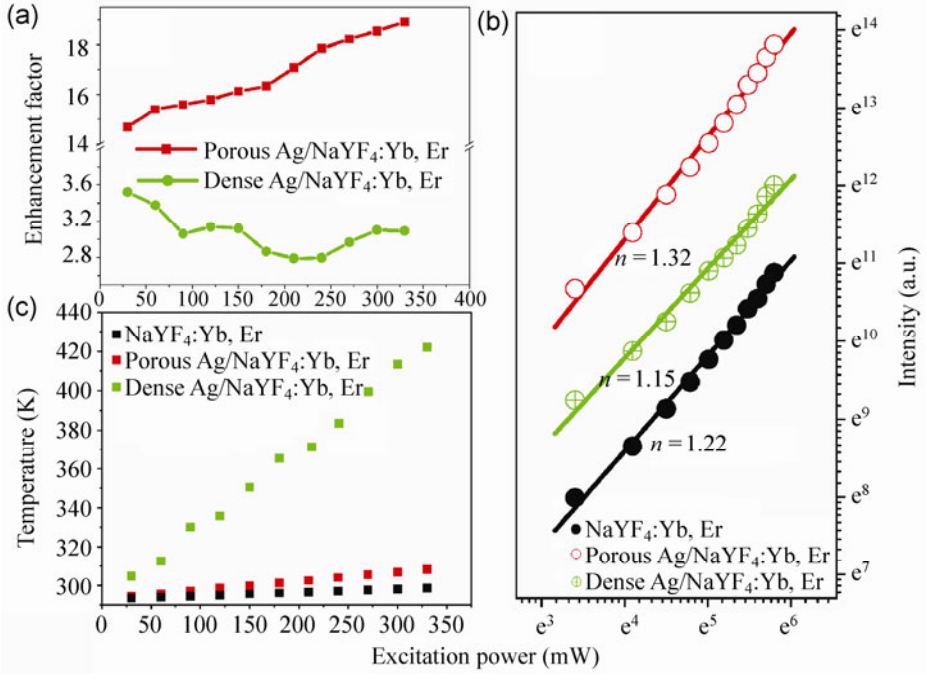

Figure 6 (a) Power-dependence of EF, (b) ln–ln plots of the $^4S_{3/2}/^2H_{11/2}$–$^4I_{15/2}$ emission intensity and (c) the deduced sample temperature based on R_{HS} of the $NaYF_4$:Yb^{3+},Er^{3+} (25 nm) film, the porous Ag/$NaYF_4$:Yb^{3+},Er^{3+} film, and the dense Ag/$NaYF_4$:Yb^{3+},Er^{3+} composite film.

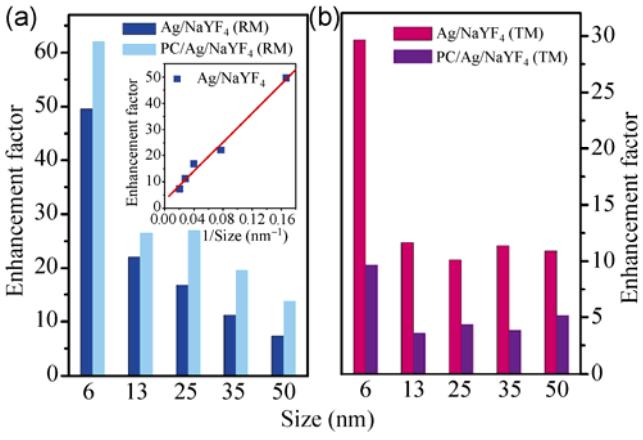

Figure 7 The size-dependence of UPL enhancement factor (EF) (collected by RM (a) and TM (b)) of porous Ag/$NaYF_4$:Yb^{3+},Er^{3+} and PC/Ag/$NaYF_4$:Yb^{3+},Er^{3+} composite films, relative to the $NaYF_4$:Yb^{3+},Er^{3+} nanofilm.

show EF as a function of $NaYF_4$:Yb^{3+},Er^{3+} particle size in porous Ag/$NaYF_4$:Yb^{3+},Er^{3+} and PMMA PC/Ag/$NaYF_4$:Yb^{3+},Er^{3+} films for RM and TM, respectively. In porous Ag/$NaYF_4$:Yb^{3+},Er^{3+} hybrids, the metal-induced UCL enhancement increased markedly with decreasing particle size. As the particle size decreased from 50 to 6 nm, EF gradually increased from ~9-fold to 50-fold compared to the $NaYF_4$:Yb^{3+},Er^{3+} film. EF was proportional to the inverse of particle size (see the inset of Fig. 7(a)), which can be attributed to the decrease in the interaction distance between the surface plasmon of silver and the UCNPs. It is well known that the maximum electric field intensity enhancement occurs mostly in the regions close to the surface of Ag NPs (within a few nanometers) and, in general, the field enhancement decays nearly exponentially with distance away from the metal surface. In other words, the maximum electric field intensity enhancement can be more effectively utilized by the smaller sized $NaYF_4$:Yb^{3+},Er^{3+} NCs, compared with the larger sized NCs, resulting in maximum UCL enhancement for the smallest $NaYF_4$:Yb^{3+},Er^{3+} NCs (~6 nm).

In the PMMA/Ag/$NaYF_4$:Yb^{3+},Er^{3+} composite film, the UCL intensity was further improved for all the samples, and the UCL enhancement reached a maximum of about ~60-fold for the hybrid consisting of ~6 nm $NaYF_4$:Yb^{3+},Er^3 NCs. In Fig. 7(b) the UCL enhancement for TM was about ~31-fold for the Ag/$NaYF_4$:Yb^{3+},Er^{3+} hybrid consisting of 6 nm $NaYF_4$:Yb^{3+},Er^{3+} and decreased to 10–12-fold when the particle size of $NaYF_4$:Yb^{3+},Er^3 ranged from 13 to 50 nm. For PMMA/Ag/$NaYF_4$:Yb^{3+},Er^{3+} hybrid films, the maximum UCL enhancement was ~10-fold for TM, lower than that in the Ag/$NaYF_4$:Yb^{3+},Er^{3+} film, indicating that the UCL intensity markedly decreased on introducing the OPC; this can be attributed to the low transmittance of PMMA OPCs in the visible region (see Fig. S2 in the ESM). It should be noted that the PMMA OPCs in the hybrid undergo far-field coupling with UCNPs, and their contribution to the UCL enhancement is to further reflect and scatter the excitation and emission light, and thus it is reasonable to observe a decrease in UCL with TM.

The angle-dependent UCL enhancement with TM was studied in order to further analyze the PC effect and the plasmon effect in the hybrid films. Figure 8(a) illustrates the angle-dependent PSB of the PMMA OPC (the angle-dependent absorption spectra are shown in Fig. S2 in the ESM). It can be observed that the PSB gradually shifted to the blue, varying from 978 to 908 nm as the incident angle ranged from 0° to 30°, which can be well fitted by the Bragg diffraction equation [30]

$$\lambda = \frac{2d_{hkl}}{m}\sqrt{n_{eff}^2 - \sin^2\theta}$$

where λ is the central wavelength of PSB, m is the order of the Bragg diffraction, d_{hkl} is the hkl plane distance (fcc $d_{111} = \sqrt{2/3}\,D$ with D being the diameter of the beads), n_{eff} is the average refractive index and θ is the angle of deviation from the normal to the hkl planes. From the Bragg diffraction equation, it can be concluded that the PSB can be tuned by changing either the bead size, or the incident angle. In the measurements, the angle between the incident light and the sample was controlled by adjusting the sample (see Scheme 1(b)) without changing the optical path. Figure 8(b) depicts the EF factor as a function of angle between the incident light and the hybrid film samples. It is interesting that for porous Ag/$NaYF_4$:Yb^{3+},Er^{3+} hybrids consisting of 6 nm and 50 nm UCNPs, the metal-induced EF gradually increased from 30-fold to 41-fold, and from 10-fold to 25-fold, respectively, as the incident angle changed from 0° to 20°. The EF reached a maximum at 20°, and then gradually

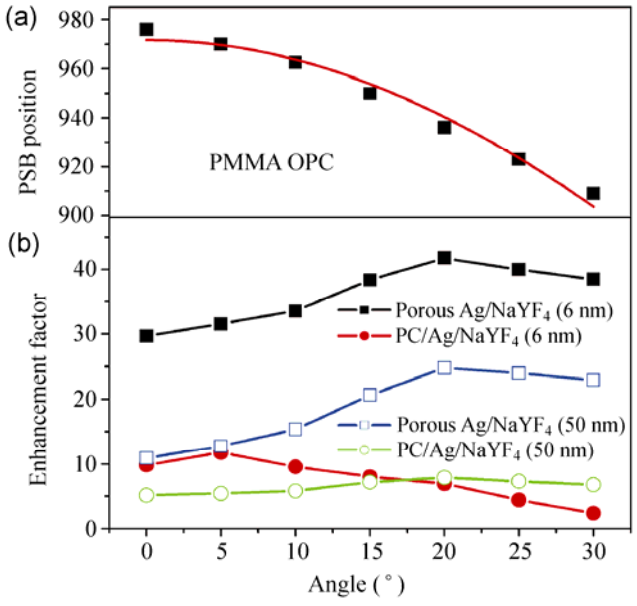

Figure 8 (a) The angle-dependent PSB of PC. (b) The angle-resolved UCL EF of TM for 6 nm and 50 nm $NaYF_4$:Yb^{3+},Er^{3+}.

decreased as the incident angle was further increased from 20° to 30°. This shows that the coupling of SPA of the porous silver with $NaYF_4$:Yb^{3+},Er^{3+} UCNPs is angle-dependent under TM. It should be highlighted that the location and strength of the SPA showed little dependence on the direction of the incident light. On the one hand, as the incident angle increased, the coupling length between SPA and the UCNPs increased, leading to improved UCL enhancement. On the other hand, the excitation power density decreased with increasing angle, resulting in a decrease in UCL enhancement. These two competing processes lead to an optimum UCL enhancement as a function of angle.

In the PMMA/Ag/$NaYF_4$:Yb^{3+},Er^{3+} hybrid film consisting of 6 nm UCNPs, the initial EF was about 10-fold for incident angles ranging of 0° to 5°, and gradually decreased to 2.4-fold as the incident angle was further increased from 5° to 30°. As the incident angle changed from 0° to 30°, the PSB of OPCs became far away from the 980 nm excitation light, resulting in the decreased coupling of the OPCs with the excitation light and the decreased transmission of visible emissions and, as a consequence, EF decreased. For the hybrid consisting of 50 nm UCNPs, the EF first increased from 5.1-fold to 7.8-fold as the incident angle was increased from 0° to 20°and reached a maximum at 20°, and then decreased to 6.8-fold when the angle was further increased from 20° to 30°. This trend is different from that for the hybrid consisting of 6 nm UCNCs but is similar to the trend for the hybrid without PMMA OPCs. The metal-induced EF for Ag/$NaYF_4$:Yb^{3+},Er^{3+} film changed 2.4-fold as the incident angle increased from 0° to 20°, suppressing the effect of the PSB on the UCL. It can be also observed that after introducing the PMMA OPC, the EF decreases because of the low transmittance of the OPC in the visible region (see Fig. S2 in the ESM), which is consistent with the results of Fig. 7.

From the results of steady state UCL measurements, we can conclude that: (1) The maximum EF was ~60-fold, obtained using the PMMA/Ag/$NaYF_4$:Yb^{3+},Er^{3+} hybrid film under RM, which combined the near-field coupling of the SPA of the Ag film and the far-field reflection and scattering of the OPC; (2) EF under RM was systematically higher than that under TM for both the Ag/$NaYF_4$:Yb^{3+},Er^{3+} and PMMA/Ag/$NaYF_4$:Yb^{3+},Er^{3+} films; (3) EF markedly increased with decreasing particle size of $NaYF_4$:Yb^{3+},Er^{3+}; (4) the angle-resolved EF for Ag/$NaYF_4$:Yb^{3+},Er^{3+} films demonstrated a maximum at 20°, showing the anisotropic nature of the coupling of the porous Ag film with the UCNPs.

2.4 Size-dependent UCL dynamics in the hybrids

In order to better understand the size-dependent UCL EF behavior in porous Ag/$NaYF_4$:Yb^{3+},Er^{3+} films, the UCL dynamic processes of the excited states ($^4S_{3/2}$, $^4F_{9/2}$) for Er^{3+} ions in different samples were measured and compared. Figure 9 records the rising and the decay time constants of the $^4S_{3/2}$/$^4F_{9/2}$–$^4I_{15/2}$ transitions of Er^{3+} ions under the excitation of a 980 nm pulsed laser, which can be well fitted to a double exponential function $I(t) = I_0 e^{-t/\tau_0} - I_1 e^{-t/\tau_1}$ [38]. It can be concluded that, in both the $NaYF_4$:Yb^{3+},Er^{3+} film and the porous Ag/$NaYF_4$:Yb^{3+},Er^{3+} composite film, that as the size of $NaYF_4$:Yb^{3+},Er^{3+} increased from 6 to 50 nm, the rising (τ_1) and decay time (τ_0) constants gradually increased for both the green and the red UCL. Because smaller NPs usually have higher surface area as well as more defect states and lower crystallinity, the decay process is faster due to improved nonradiative transitions, leading to the lower quantum efficiency of UCL.

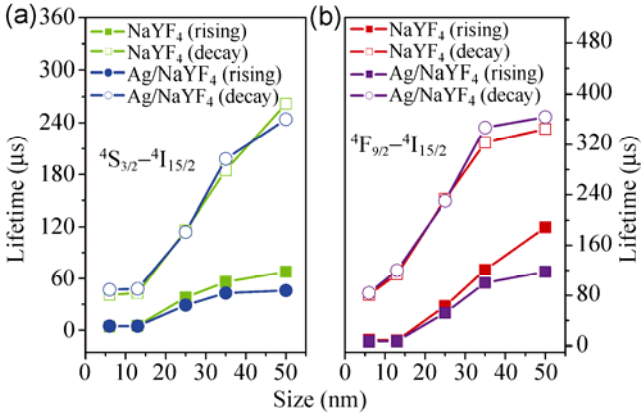

Figure 9 The size-dependence of the UCL lifetimes including the rising and the decay time constants of the $^4S_{3/2}/^4F_{9/2}$–$^4I_{15/2}$ transitions for Er^{3+} ions in the $NaYF_4$ film and porous Ag/$NaYF_4$:Yb^{3+},Er^{3+} composite film under the excitation of a 980 nm pulsed laser.

It should be highlighted that in comparison to pure $NaYF_4$:Yb^{3+},Er^{3+} NPs, the decay time constants of the $^4S_{3/2}/^4F_{9/2}$–$^4I_{15/2}$ transitions for porous Ag/$NaYF_4$:Yb^{3+},Er^{3+} composite films showed little size-dependence, with the maximum variation being lower than 8%. This suggests that for the emission levels, the radiative and nonradiative transition rates were essentially constant. However, in the Ag/$NaYF_4$:Yb^{3+},Er^{3+} composite films the rising time constants were all slightly lower than the corresponding values for $NaYF_4$:Yb^{3+},Er^{3+} NPs, for both the green and red emissions. From previous work [38], we know that the rising processes of the dynamics are dominated by the $^2F_{5/2}$–$^2F_{7/2}$ decay rate of Yb^{3+}, the total electron transfer (ET) rate from Yb^{3+} to Er^{3+} and the nonradiative relaxation rate of $^4F_{7/2}$–$^2H_{11/2}/^4S_{3/2}$. Any increase in these rates will result in decreasing rising time constants. Because the energy gap between $^4F_{7/2}$ and $^2H_{11/2}/^4S_{3/2}$ (1,500 cm^{-1}) is very small, we believe that in the Ag/$NaYF_4$:Yb^{3+},Er^{3+} composite film, the nonradiative relaxation rate of $^4F_{7/2}$–$^2H_{11/2}/^4S_{3/2}$ will increase due to metal-induced thermal effects. Considering that the porous Ag film had a broad surface plasmon resonance (SPR) ranging from 350–1,100 nm overlapping with all the emissions of $NaYF_4$:Yb^{3+},Er^{3+} in this range (including $^2F_{5/2}$–$^2F_{7/2}$ of Yb^{3+} at 980 nm) and the decay time constants of the red and green emissions for Er^{3+} are nearly constant, we deduce that the transition rate of $^2F_{5/2}$–$^2F_{7/2}$ for Yb^{3+} should also only change slightly. This indicates that the remarkable UCL enhancement was mainly induced by the coupling of the 980 nm excitation light with the SPR and/or the PSB of OPCs, rather than an increase in radiative transition rates of Er^{3+}/Yb^{3+} ions due to the coupling of SPA of silver with emitted light.

Generally speaking, because of the high extinction cross section of metal NPs, an intervening layer with a thickness of about 10 nm between the metal NPs and UPNCs is needed to prevent ET from the luminescent center to the metal NPs leading to the fast nonradiative relaxation of the luminescent center. It should be highlighted that in our porous Ag/$NaYF_4$:Yb^{3+},Er^{3+} hybrid films, we did not observe any obvious increase in nonradiative relaxation for the emission levels even although there was no intervening layer. This is mainly due to the porous Ag film being mostly composed of particles with a size of hundreds of nanometers to several micrometers, in which the scattering cross section of silver particles was much larger than the absorption cross section. Thus, even in the absence of an intervening layer, a remarkable luminescence enhancement was achieved.

2.5 Luminescent enhancement for down-conversion

In order to provide a complete understanding of the luminescent enhancement behavior of the porous Ag/$NaYF_4$:Yb^{3+},Er^{3+} hybrid films, down-conversion experiments with different excitation wavelengths were also performed. The dependence of EF on excitation wavelength (ranging from 400–550 nm) for $^4S_{3/2}$–$^4I_{15/2}$ and $^4F_{9/2}$–$^4I_{15/2}$ transitions in porous Ag/$NaYF_4$:Yb^{3+},Er^{3+} films consisting of 25 nm UCNPs is shown in Figs. 10(a) and 10(b), respectively. In the excitation spectra, the three groups of excitation lines in the ranges 435–445 nm, 475–485 nm and 520–540 nm, correspond to the $^4I_{15/2}$–$^4F_{5/2}$, $^4F_{7/2}$ and $^2H_{11/2}$ transitions, respectively. For green and red emissions, the EF changed randomly in the range of 2–5-fold as the excitation wavelength was varied in the range 400–550 nm. The average enhancement for the red emission (averaged EF = 3.0) was slightly higher than that for the green emission (averaged EF = 2.5). However, the EFs under photon down-conversion excitation are much smaller than those under photon UC excitation. For the visible light excitation shown in Fig. 10, the green and red emissions originate from a one-photon process, while for 980 nm excitation a

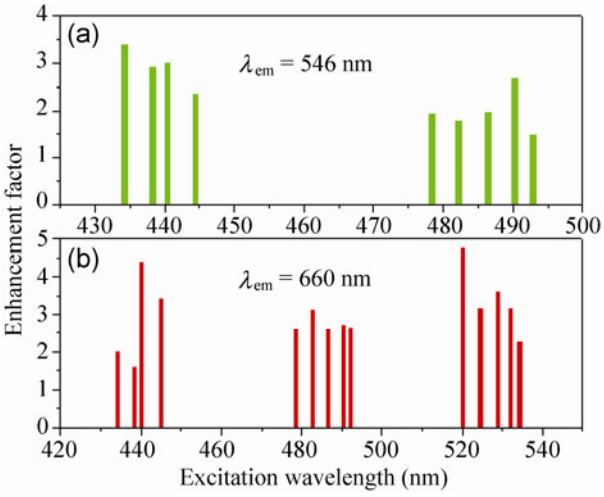

Figure 10 The excitation wavelength (ranging from 400–550 nm) dependence of EF for $^4S_{3/2}$–$^4I_{15/2}$ (a) and $^4F_{9/2}$–$^4I_{15/2}$ (b) transitions in the porous Ag/$NaYF_4$:Yb^{3+},Er^{3+} film relative to the $NaYF_4$:Yb^{3+},Er^{3+} (25 nm) film.

two-photon UC process is involved. Theoretically, the emission intensity for down-conversion luminescence is proportional to the excitation power (P), while the emission intensity for two-photon UCL is proportional to the square of excitation power (P^2) [20, 42]. Thus, it is easy to understand that under visible excitation the EF of porous Ag/$NaYF_4$:Yb^{3+},Er^{3+} is much smaller than that under 908 nm excitation.

3 Conclusions

In this work, we first prepared a porous plasmon silver film consisting of randomly distributed silver NPs (> 100 nm) by a simple PMMA template method and then studied its coupling with $NaYF_4$:Yb^{3+},Er^{3+} UCNPs with controllable sizes in order to obtain stable, reproducible and effective UCL enhancement. Firstly, it is worth highlighting that the porous structure of the silver film/$NaYF_4$:Yb^{3+},Er^{3+} composite is for the key to obtaining highly enhanced UCL, since it can not only decrease the effective interaction distance between the UCNPs and the silver film, but can also suppress local thermal effects induced by laser irradiation and increase the transparency of the film. Secondly, we studied the impact of $NaYF_4$:Yb^{3+},Er^{3+} particle size and incident angle on the UCL enhancement factor and observed that the UCL enhancement was proportional to the inverse of particle size, and that there was an optimum incident angle. Thirdly, we demonstrated that combining the near-field coupling of the porous silver film, and the far-field coupling of the three-dimensional PMMA opal photonic crystals with the UCNPs, the UCL could be further improved, with the extent depending on the particle size of UCNPs. A maximum enhancement of 60-fold was obtained, based on the coupling of silver with the UCNPs. Overall, this work is significant in offering an elementary understanding of the UCL enhancement of nanophosphors through coupling with the SPA of noble metals, and furthermore the hybrid film may have great potential applications in photoelectric devices.

Acknowledgements

This work was supported by the National Talent Youth Science Foundation of China (Grant No. 60925018), the National Natural Science Foundation of China (Grant Nos. 61204015, 51002062, 11174111, 61177042, and 81201738) and the China Postdoctoral Science Foundation Funded Project (No. 2012M511337).

Electronic Supplementary Material: Supplementary material (sample preparation methods, instrumental details, the absorption spectra of the porous Ag film with different densities of Ag and the dense film, and the incidence angle dependence of transmission spectra of PC) is available in the online version of this article at http://dx.doi.org/10.1007/s12274-013-0358-y.

References

[1] Auzel, F. Upconversion and anti-stokes processes with f and d ions in solids. *Chem. Rev.* **2004**, *104*, 139–174.

[2] Danger, T.; Koetke, J.; Brede, R.; Heumann, E.; Huber, G.; Chai, B. H. T. Spectroscopy and green upconversion laser emission of Er^{3+}-doped crystals at room temperature. *J. Appl. Phys.* **1994**, *76*, 1413–1422.

[3] Huang, X. Y.; Han, S. Y.; Huang, W.; Liu, X. G. Enhancing solar cell efficiency: The search for luminescent materials as spectral converters. *Chem. Soc. Rev.* **2013**, *42*, 173–201.

[4] Su, L. T.; Karuturi, S. K.; Luo, J. S.; Liu, L. J.; Liu, X. F.; Guo, J.; Sum, T. C.; Deng, R. R.; Fan, H. J.; Liu, X. G. et al. Photon upconversion in hetero-nanostructured photoanodes for enhanced near-infrared light harvesting. *Adv. Mater.* **2013**, *25*, 1603–1607.

[5] Aarts, L.; van der Ende, B. M.; Meijerink, A. Downconversion for solar cells in $NaYF_4$:Er,Yb. *J. Appl. Phys.* **2009**, *106*, 023522.

[6] Yu, X. F.; Li, Min.; Xie, M. Y.; Chen, L. D.; Li, Y.; Wang, Q. Q. Dopant-controlled synthesis of water- soluble hexagonal $NaYF_4$ nanorods with efficient upconversion fluorescence for multicolor bioimaging. *Nano Res*. **2010**, *3*, 51–60.

[7] Tu, D.; Liu, L. Q.; Ju, Q.; Liu,Y. S.; Zhu, H. M.; Li, R. F.; Chen, X. Y. Time-resolved FRET biosensor based on amine-functionalized lanthanide-doped $NaYF_4$ nanocrystals. *Angew. Chem. Int. Ed.* **2011**, *50*, 6306–6310.

[8] Esterowitz, L.; Noonan, J.; Bahler. J. Erratum: Enhancement in a Ho^{3+}-Yb^{3+} quantum counter by energy transfer. *Appl. Phys. Lett.* **1967**, *11*, 72.

[9] Rapaport, A.; Milliez, J.; Bass, M.; Cassanho, A.; Jenssen, J. Review of the properties of up-conversion phosphors for new emissive displays. *J. Disp. Technol.* **2006**, *2*, 68–78.

[10] Boyer, J. C.; van Veggel, F. C. J. M. Absolute quantum yield measurements of colloidal $NaYF_4$:Er^{3+},Yb^{3+} upconverting nanoparticles. *Nanoscale* **2010**, *2*, 1417–1419.

[11] Yang, T. S.; Sun, Y.; Liu, Q.; Feng, W.; Yang, P. Y.; Li, F. Y. Cubic sub-20 nm NaLuF4-based upconversion nanophosphors for high-contrast bioimaging in different animal species. *Biomaterials* **2012**, *33*, 3733–3742.

[12] Yi, G. S.; Chow, G. M. Water-soluble $NaYF_4$:Yb,Er(Tm)/$NaYF_4$/polymer core/shell/shell nanoparticles with significant enhancement of upconversion fluorescence. *Chem. Mater.* **2007**, *19*, 341–343.

[13] Wang, F.; Deng, R. R.; Wang, J.; Wang, Q. X.; Han, Y.; Zhu, H. M.; Chen, X. Y.; Liu, X. G. Tuning upconversion through energy migration in core–shell nanoparticles. *Nat. Mater.* **2011**, *10*, 968–973.

[14] Ming, T.; Chen, H. J.; Jiang, R. B.; Li, Q.; Wang, J. F. Plasmon-controlled fluorescence: Beyond the intensity enhancement. *J. Phys. Chem. Lett.* **2012**, *3*, 191−202.

[15] Viste, P.; Plain, J.; Jaffiol, R.; Vial, A.; Adam, P. M.; Royer, P. Enhancement and quenching regimes in metal-semiconductor hybrid optical nanosources. *ACS nano* **2010**, *4*, 759–764.

[16] Bharill, S.; Chen, C. L.; Stevens, B.; Kaur, J.; Smilansky, Z.; Mandecki, W.; Gryczynski, I.; Gryczynski, Z.; Cooperman, B. S.; Goldman, Y. E. Enhancement of single-molecule fluorescence signals by colloidal silver nanoparticles in studies of protein translation. *ACS nano* **2011**, *5*, 399–407.

[17] Schietinger, S.; Aichele, T.; Wang, H. Q.; Nann, T.; Benson, O. Plasmon-enhanced upconversion in single $NaYF_4$:Yb^{3+}/Er^{3+} codoped nanocrystals. *Nano Lett* **2010**, *10*, 134–138.

[18] Zhang, F.; Braun, G. B.; Shi, Y. F.; Zhang, Y. C.; Sun, X. H.; Reich, N. O.; Zhao, D. Y.; Stucky, G. Fabrication of Ag@SiO_2@Y_2O_3:Er nanostructures for bioimaging: Tuning of the upconversion fluorescence with silver nanoparticles. *J. Am. Chem. Soc.* **2010**, *132*, 2850–2851.

[19] Zhang, H.; Li, Y. J.; Ivanov, I. A.; Qu, Y. Q.; Huang, Y.; Duan, X. F. Plasmonic modulation of the upconversion fluorescence in $NaYF_4$:Yb/Tm hexaplate nanocrystals using gold nanoparticles or nanoshells. *Angew. Chem. Int. Ed.* **2010**, *49*, 2865–2868.

[20] Liu, N.; Qin, W. P.; Qin, G. S.; Jiang, T.; Zhao, D. Highly plasmon-enhanced upconversion emissions from Au@β-$NaYF_4$:Yb,Tm hybrid nanostructures. *Chem. Commun.* **2011**, *47*, 7671–7673.

[21] Priyam, A.; Idris, N. M.; Zhang, Y. Gold nanoshell coated $NaYF_4$ nanoparticles for simultaneously enhanced upconversion fluorescence and darkfield imaging. *J. Mater. Chem.* **2012**, *22*, 960–965.

[22] Zhang, W. H.; Ding, F.; Chou, S. Y. Large enhancement of upconversion luminescence of $NaYF_4$:Yb^{3+}/Er^{3+} nanocrystal by 3D plasmonic nano-antennas. *Adv. Mater.* **2012**, *24*, OP236–OP241.

[23] Saboktakin, M.; Ye, X. C.; Oh, S. J.; Hong, S. H.; Fafarman, A. T.; Chettiar, U. K.; Engheta, N.; Murray, C. B.; Kagan, C. R. Metal-enhanced upconversion luminescence tunable through metal nanoparticle-nanophosphor separation. *ACS nano* **2012**, *6*, 8758–8766.

[24] Fujii, M.; Nakano, T.; Imakita, K.; Hayashi, S. Upconversion luminescence of Er and Yb codoped $NaYF_4$ nanoparticles with metal shells. *J. Phys. Chem. C* **2013**, *117*, 1113−1120.

[25] Paudel, H. P.; Zhong, L. L.; Bayat, K.; Baroughi, M. F.; Smith, S.; Lin, C. K.; Jiang, C. Y.; Berry, M. T.; May, P. S. Enhancement of near-infrared-to-visible upconversion luminescence using engineered plasmonic gold surfaces. *J. Phys. Chem. C* **2011**, *115*, 19028–19036.

[26] Xu, W.; Xu, S.; Zhu, Y. S.; Liu, T.; Bai, X.; Dong, B.; Xu, L.; Song, H. W. Ultra-broad plasma resonance enhanced multicolor emissions in an assembled Ag/$NaYF_4$:Yb, Er nano-film. *Nanoscale* **2012**, *4*, 6971–6973.

[27] Evanoff Jr, D. D.; Chumanov, G. Synthesis and optical properties of silver nanoparticles and arrays. *ChemPhysChem* **2005**, *6*, 1221–1231.

[28] Ogawa, S.; Imada, M.; Yoshimoto, S.; Okano, M.; Noda, S. Control of light emission by 3D photonic crystals. *Science* **2004**, *305*, 227–229.

[29] Joannopoulos, J. D.; Johnson, S. G.; Winn, J. N.; Meade, R. D. *Photonic Crystals Molding the Flow of Light*; Princeton University Press: Princeton, 2008.

[30] Wang, W.; Song, H. W.; Bai, X.; Liu, Q.; Zhu, Y. S. Modified spontaneous emissions of europium complex in weak PMMA opals. *Phys. Chem. Chem. Phys.* **2011**, *13*, 18023–18030.

[31] Tao, C. A.; Zhu, W.; An, Q.; Yang, H. W.; Li, W. N.; Lin, C. X.; Yang, F. Z.; Li, G. T. Coupling of nanoparticle plasmons with colloidal photonic crystals as a new strategy to efficiently enhance fluorescence. *J. Phys. Chem. C* **2011**, *115*, 20053–20060.

[32] Li, Z. Q.; Wang, L. M.; Wang, Z. Y.; Liu, X. H.; Xiong, Y. J. Modification of $NaYF_4$:Yb, Er@SiO_2 nanoparticles with gold nanocrystals for tunable green-to-red upconversion emissions. *J. Phys. Chem. C* **2011**, *115*, 3291–3296.

[33] Wu, Y.; Shen, X.; Dai, S. X.; Xu, Y. S.; Chen, F. F.; Lin, C. G.; Xu, T. F.; Nie, Q. H. Silver nanoparticles enhanced upconversion luminescence in Er^{3+}/Yb^{3+} codoped bismuth-germanate glasses. *J. Phys. Chem. C* **2011**, *115*, 25040–25045.

[34] Li, Z. Q.; Zhang, Y. An efficient and user-friendly method for the synthesis of hexagonal-phase $NaYF_4$:Yb,Er/Tm nanocrystals with controllable shape and upconversion fluorescence. *Nanotechnology* **2008**, *19*, 345606.

[35] Wiley, B.; Sun, Y. G.; Xia, Y. N. Synthesis of silver nanostructures with controlled shapes and properties. *Acc. Chem. Res*. **2007**, *40*, 1067–1076.

[36] Kinnan, M. K.; Chumanov, G. Plasmon coupling in two-dimensional arrays of silver nanoparticles: II. effect of the particle size and interparticle distance. *J. Phys. Chem. C* **2010**, *114*, 7496–7501.

[37] Wang, Y.; Tu, L. P.; Zhao, J. W.; Sun, Y. J.; Kong, X. G.; Zhang, H. Upconversion luminescence of β-$NaYF_4$:Yb^{3+}, Er^{3+}@β-$NaYF_4$ core/shell nanoparticles: Excitation power density and surface dependence. *J. Phys. Chem. C* **2009**, *113,* 7164–7169.

[38] Li, D.; Dong, B.; Bai, X.; Wang, Y.; Song, H. W. Influence of the TGA modification on upconversion luminescence of hexagonal-phase $NaYF_4$:Yb^{3+},Er^{3+} nanoparticles. *J. Phys. Chem. C* **2010,** *114,* 8219–8226.

[39] Bai, X.; Song, H. W.; Pan, G. H.; Lei, Y. Q.; Wang, T.; Ren, X. G.; Lu, S. Z.; Dong, B.; Dai, Q. L.; Fan, L. B. Size-dependent upconversion luminescence in Er^{3+}/Yb^{3+}-codoped nanocrystalline Yttria: Saturation and thermal effects. *J. Phys. Chem. C* **2007**, *111*, 13611–13617.

[40] Pollnau, M.; Gamelin, D. R.; Luthi, S. R.; Gudel, H. U. Power dependence of upconversion luminescence in lanthanide and transition-metal-ion systems. *Phys. Rev. B* **2000**, *61*, 3337–3346.

[41] Dai, Q. L.; Song, H. W.; Ren, X. G.; Lu, S. Z.; Pan, G. H.; Bai, X.; Dong, B.; Qin, R. F.; Qu, X. S.; Zhang, H. Structure and upconversion luminescence of hydrothermal $PbWO_4$:Er^{3+},Yb^{3+} powders. *J. Phys. Chem. C* **2008**, *112*, 19694–19698.

[42] Fischer, J.; Bocchio, N.; Unger, A.; Butt, H. J.; Koynov, K.; Kreiter, M. Near-field-mediated enhancement of two-photon-induced fluorescence on plasmonic nanostructures. *J. Phys. Chem. C* **2010**, *114*, 20968–20973.